Carbon 196 (2022) 378–390

Contents lists available at ScienceDirect

Carbon

journal homepage: www.elsevier.com/locate/carbon

Efficient and cost-effective ORR electrocatalysts based on low content transition metals highly dispersed on C_3N_4/super-activated carbon composites

G. Alemany-Molina [a], J. Quílez-Bermejo [a], M. Navlani-García [a], E. Morallón [b], D. Cazorla-Amorós [a,*]

[a] Department of Inorganic Chemistry and Materials Institute, University of Alicante, Ap. 99, Alicante, E-03080, Spain
[b] Department of Physical Chemistry and Materials Institute, University of Alicante, Ap. 99, Alicante, E-03080, Spain

ARTICLE INFO

Keywords:
Carbon nitride
Copper
Iron
Activated carbon
ORR

ABSTRACT

Oxygen reduction reaction (ORR) is one of the most important electrochemical reactions for fuel cells. However, commercial Pt-based catalysts used have important limitations such as their deactivation by carbon monoxide and Pt scarcity. In the present work, small and highly-dispersed copper and iron clusters were anchored onto composite supports based on carbon nitride (C_3N_4) nanostructures and a highly porous carbon material. Catalysts with a moderate carbon nitride content showed an interesting catalytic behaviour because of the combination of the metallic active sites and the availability of micropores, which play an active role in ORR. The presence of either Fe or Cu in the synthesis affected the structure of the resulting composite materials, as well as their electrocatalytic activity. Copper-based materials showed superior catalytic activity, which is supported by the information obtained from the evaluation of the system using DFT computational calculations.

1. Introduction

The necessity to reduce the use of fossil fuels has led to an important energy crisis that can only be reversed with the implementation of renewable energies [1,2]. Fuel cells using hydrogen as an energy vector appear as an attractive alternative to facilitate the implementation of renewable energies, but this technology is not being commercialized on a large scale due to some factors that affect their performance and efficiency [3]. The most efficient catalyst for the oxidation of hydrogen and the oxygen reduction reaction (ORR) in the fuel cell is based on platinum nanoparticles supported on carbon materials, usually carbon black [4]. The ORR remains a significant bottleneck because it shows sluggish kinetics and significant overpotentials, which requires high platinum loadings in the cathode of the fuel cells (0.4 mg/cm^2 versus 0.05 mg/cm^2 in the anode) [5]. Owing to the scarcity of platinum in the Earth's crust, finding new materials to substitute this precious metal is critical for the implementation of this technology [6].

In the last years, heterogeneous catalysts based on single-atom (SACs) or few-atom metal clusters have arisen interest in industrial catalysis due to the high activities observed and the efficient metal atom utilisation [7–9]. These materials allow to downsize considerably the noble-metal loading in the catalysts or even substitute noble-metal atoms by transition metals maintaining the catalytic activity of the state-of-the-art electrodes [7]. Few-atom metal clusters and SACs have been successfully applied in thermo-catalysis, photocatalysis and electrocatalysis, noting some excellent catalytic performance as ORR catalysts [10–13]. As for carbon-based materials, single metal sites have been supported over carbon materials (e.g. CNT) [14,15], inserted into the carbon structure of amorphous porous N-doped carbons [11,13] or, as it has been recently reported, introduced in the graphene layers of molecular-level ordered structures in ordered carbonaceous frameworks [16]. More specifically, SACs based on iron [15,17–19] and copper [20–24] supported on N-doped carbon materials have demonstrated great potential as substitutes for the commercial Pt-catalysts. However, these catalysts are usually obtained from multi-step synthesis protocols that require harsh conditions and nitrogen species are found in low concentrations [25]. On Fe or Cu SACs based on N-containing carbon materials, the resultant structure of the catalysts usually consists of the

* Corresponding author. Departamento de Química Inorgánica e Instituto Universitario de Materiales, University of Alicante, P.O. Box 99, San Vicente del Raspeig, E-03080, Alicante, Spain.
E-mail address: cazorla@ua.es (D. Cazorla-Amorós).

https://doi.org/10.1016/j.carbon.2022.05.003
Received 28 February 2022; Received in revised form 14 April 2022; Accepted 1 May 2022
Available online 11 May 2022

metal bonded to four nitrogen atoms, leaving the axial position free for the O_2 chemisorption [8]. These materials based on Fe and Cu have also shown interesting results in other important electrochemical reactions of great importance from the environmental point of view, such as hydrogen evolution reaction (HER) [26,27], nitrogen reduction reaction (NRR) [28–30], or CO_2 reduction reaction (CO_2RR) [31–35].

Carbon nitride (C_3N_4) presents a well-defined structure with interesting properties as a single-atom or ultra-small metal cluster host because of the presence of basic nitrogen-based Lewis surface sites where single atoms are easily anchored [18,36]. The location of metal atoms in the internal C_3N_4 cavities has been proved to be energetically favourable by theoretical studies [37–39]. However, because of the tendency to stacking of C_3N_4 layers, this material presents a low surface area (~10 m^2/g) compared to other carbon-based electrocatalyst supports such as carbon black (240 m^2/g of Vulcan) [40], which makes difficult the full utilization of the metal-ligand sites. To solve this limitation, C_3N_4 is frequently combined with other carbon-based materials forming hybrids or composite materials to achieve materials with enhanced textural properties [41–43]. Moreover, π-π interaction between the carbon material and C_3N_4 induces electronic delocalization, which can lead to improved electrocatalytic performance [44,45].

In this work, highly dispersed Fe and Cu atoms anchored on composite supports based on C_3N_4-type nano-domains and an activated carbon with exceptional textural properties (BET surface area >3000 m^2/g) were developed by using a simple one-pot process and a reproducible synthetic protocol. To the best of our knowledge, this C_3N_4/C composite material has not been studied before as a transition metal support for ORR electrocatalysts. The combination of the C_3N_4, offering excellent anchoring points for the metal species, and a highly microporous activated carbon, can boost the catalytic activity of Fe and Cu single atoms and few-atoms clusters. The catalytic properties were evaluated towards the ORR and the experimental results were supported by Density Functional Theory (DFT) calculations, pointing out the key role of the metal species anchored to C_3N_4 sites in the ORR, especially in an alkaline electrolyte.

2. Experimental

2.1. Materials

Spanish Anthracite "Anita", 1 mm; Potassium hydroxide in pellets (KOH, 85% WWR Chemicals); Copper (II) nitrate 3-hydrate ($Cu(NO_3)_2{\cdot}3H_2O$, 99%, Panreac); Iron (III) nitrate 9-hydrate ($Fe(NO_3)_3{\cdot}9H_2O$, 99.99%, Sigma Aldrich); Dicyandiamide ($C_2H_4N_4$, Wako Pure Chemical Industries); Methanol (CH_3OH, 99.99%, Sigma Aldrich); 2-Propanol (C_3H_8O, 99.9%, Supelco); Nafion D-520 dispersion 5% w/w in water; 1-propanol (Alfa Aesar).

2.2. M-C_3N_4/KUA preparation

The activated carbon material used as support (KUA) was prepared through chemical activation of an anthracite with KOH following the method described by Lozano-Castelló et al. [46] The Fe and Cu–C_3N_4/KUA catalysts were synthesized using the as-prepared KUA and dicyandiamide as the C_3N_4 precursor. For that, 0.3 g of KUA were mixed with variable amounts of dicyandiamide (15, 30, and 50 wt% of the initial total mass). Then, the required amount of the metal precursor ($Fe(NO_3)_3$ or $Cu(NO_3)_2$) was added to achieve a nominal metal loading of 1 wt%. The resulting mixture was dispersed in 2 mL of water by sonicating in an ultrasound bath for 15 min. After that, water was removed by evaporation until dryness. Next, the samples were subjected to a 4 h heat treatment at 520 °C, with a heating rate of 5 °C/min and 150 mL/min of N_2-atmosphere. The synthetic protocol is summarized in Scheme 1. The nomenclature used for the electrocatalysts was M-C3N4/KUA_XX, where M is the metal (Fe or Cu) and XX is the dicyanamide weight percentage used in the synthesis (15, 30, and 50 wt %). For comparison purposes, samples without metal (C3N4/KUA_XX) and samples without C_3N_4 (Cu/KUA and Fe/KUA) were prepared following the same synthesis conditions. Moreover, a sample of C_3N_4 without KUA was synthesized and a sample of KUA was subjected to a 1 h heat treatment at 900 °C (KUA(900)), with a heating rate of 5 °C/min and 100 mL/min of N_2-atmosphere. This heat treated sample has been used in the synthesis protocol for the preparation of Cu–C3N4/KUA (900)_15 sample.

2.3. Characterisation

The surface chemistry was evaluated by temperature programmed desorption (TPD) experiments using a DSC-TGA instrument (TA Instruments, SDT 600 Simultaneous) coupled to a mass spectrometer (PRISMA PRO QMG 250 M1). The carrier gas used was He (100 mL min^{-1}) and the samples were heated from 120 °C to 950 °C, with a heating rate of 20 °C·min^{-1}. They were previously dried at 120 °C for 1 h. The nitrogen content was determined by elemental analysis using a Thermo Finnigan Flash 1112 Series microanalyser. Metal content was determined by inductively coupled plasma-optical emission spectroscopy (ICP-OES) using a Perkin-Elmer Optima 4300 system. X-ray diffraction (XRD) analysis was carried out at room temperature with a Bruker X-ray Diffractometer (D8-Advance model) provided with a Göebel mirror and a Kristalloflex X-ray generator (K 760-80F model) with Cu Kα radiation and a scanning rate of 2°/min, in the range of 10–80°. TEM micrographs were recorded with a transmission electron microscope model JEOL JEM-2010 (200 kV). Nitrogen adsorption-desorption isotherms were performed at −196 °C in the adsorption gases instrument ASAP 2020. Before the analysis, the samples were

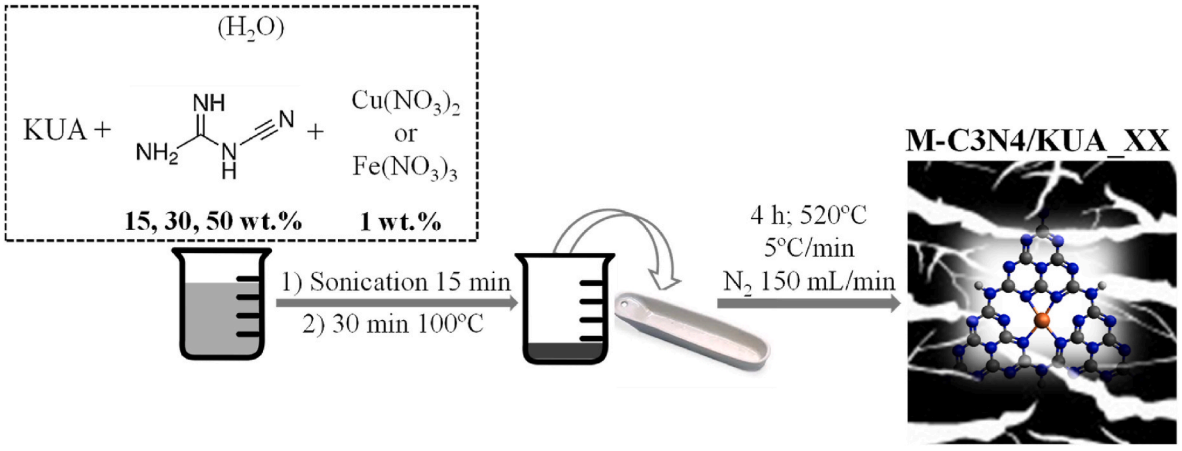

Scheme 1. M-C3N4/KUA_XX synthesis.

degassed at 250 °C under high vacuum for 4 h. For the analysis of the results, BET (Brunauer, Emmett and Teller) method [47] was applied for the calculation of the apparent surface area (S_{BET}). Furthermore, non-localised density functional theory (NL-DFT) [48,49] was applied to calculate the pore size distribution (PSD) using SAIEUS software (available online at http://www.nldft.com/) [50]. The volume of micropores was estimated as the volume accumulated until w = 2 nm in the NLDFT analysis (V_{micro}). The total pore volume (V_t) was calculated at a relative pressure of $P/P_0 = 0.99$. The amount of guest (C_3N_4) was estimated from the synthesis yields and was used to calculate the S_{BET} with the mixtures law. The pore volume of KUA filled with C_3N_4 was estimated as the difference between V_t of KUA and the volume of C_3N_4 ($V_{t\,KUA} - m_{C3N4}/\rho_{C3N4}$), where m_{C3N4} is the weight of C_3N_4 in the sample and ρ_{C3N4} is the density of C_3N_4. The density used for ρ_{C3N4} was 2.336 g cm^{-3} [51]. X-ray Photoelectron Spectroscopy (XPS) was used to analyse the surface composition using a K-α spectrometer from Thermo Scientific, equipped with an Al anode.

2.4. Electrochemical characterisation

Electrochemical characterisation of the samples was studied by cyclic voltammetry (CV) in a N_2-saturated 0.1 M KOH solution using an Autolab PGSTAT302 potentiostat. A rotating disk electrode (RDE) equipped with a glassy carbon disk electrode (5 mm diameter) was used as a working electrode, while a hydrogen reversible electrode was used as a reference electrode, and a graphite bar as the counter electrode. The glassy carbon disk was modified with the samples through the drop-casting of 120 μg of the samples. Thus, 120 μL of a 1 mg/mL suspension (4% Nafion, 20% isopropanol in water) were deposited onto the disk electrode.

The ORR catalytic activity was studied through Linear Sweep Voltammetry (LSV) in a potential range between 1 and 0 V vs. RHE in an oxygen-saturated 0.1 M KOH solution. Koutecky-Levich analysis [52] was applied to determine the number of electrons transferred (n_{KL}) during ORR measurements. The percentage of H_2O_2 generated was estimated from the number of electrons transferred. The onset potential of this reaction was measured at −0.1 mA/cm^2 and it was also calculated by the tangent method. Furthermore, stability studies were performed by means of chronoamperometric assays at a constant potential of 0.65 V vs RHE at 1600 rpm for 4 h. Poisoning resistance was evaluated by the addition of methanol to the electrochemical cell to reach a 1 M methanol solution and the percentage of initial current versus time was recorded.

A commercial Pt (20 wt%) on graphitised carbon (Sigma-Aldrich) was used as a reference electrocatalyst in LSV (Pt/C).

2.5. Computational calculations

Density Functional Theory (DFT) calculations at B3LYP/6-31g level using Gaussian 09 software were carried out to understand and support the observed experimental results. Moreover, in order to reproduce as accurately as possible the chemical environment where the reaction takes place, a polarized continuum model (PCM) was applied with the dielectric constant of water. The model structures consist of a basic C_3N_4 unit formed by 3 heptazine units that offer 6 basic nitrogens to the metallic atom located in the internal cavity [25].

Pourbaix diagrams of M-C3N4 flakes were calculated to elucidate the initial composition and configuration of the catalyst before ORR occurs. Diagrams were obtained according to Heine et al. [53] The ORR energy diagrams were computed according to Norskov model [54]. For the calculation of the free energy change for each reaction stage, the free energies were calculated including vibrational corrections. Free-energy diagrams for the 4 and the 2-electron mechanisms were elaborated to obtain information about the limiting step and the selectivity of the reaction.

3. Results and discussion

3.1. Characterisation of the samples

Synthesis yields are presented in Table 1. The C_3N_4 formation yield from pristine dicyandiamide was determined to be 50%. The amount of CO and CO_2 groups of bare KUA was evaluated by TPD experiments resulting in 2350 μmol g^{-1} and 360 μmol g^{-1}, respectively. When KUA is heated up to 520 °C for 4 h, the yield was 92% owing to the desorption of oxygen functional groups. According to the relative proportion of C_3N_4 and KUA in the composites, yields of 86, 79, and 71% would be expected for C3N4/KUA_15, C3N4/KUA_30, and C3N4/KUA_50, respectively, which are close to the experimental values attained. For equal amounts of precursor, the yields obtained were similar for the three samples (i.e. C3N4/KUA_XX, Fe–C3N4/KUA_XX, and Cu–C3N4/KUA_XX), so the carbonisation yields of the samples are mainly related to the dicyandiamide decomposition reactions that lead to the formation of C_3N_4-type structures, and to the decomposition of some KUA surface oxygen groups. The nitrogen content (%N (at. %)) determined by elemental analysis increased proportionally to the amount of dicyandiamide used in the synthesis of the samples, and the metal content determined by ICP is slightly higher than the nominal 1 wt% (Table 1). Comparing the total N and M contents, the N/M atomic ratios for copper samples were 8.0, 10.0, and 13.4 while for iron samples were 4.7, 8.5, and 18.1, for the samples with 15, 30 and 50% of C_3N_4 precursor, respectively.

Fig. 1 includes the diffractograms of all the composites studied as well as that of bare C_3N_4 for comparison purposes. The diffractogram of C_3N_4 showed a main peak at 27° due to the reflection from the plane (002) of graphitic carbon nitride and a small peak at 13°, which corresponds to (100) plane [55]. The (002) contribution appears in C3N4/KUA_50 as a broad peak due to the presence of low-crystallinity carbon nitride [41]. This broad peak is also observed for the metal-containing samples prepared for the different C_3N_4 contents (Fig. 1). This broad contribution indicates that, in the presence of KUA and also metal species, dicyandiamide is not producing large C_3N_4 sheets, but heterogeneous C_3N_4-type nanodomains that are well distributed inside the abundant micropores of the activated carbon used, which are most probably located on the graphene-type pore walls of the carbon material. M-C3N4/KUA samples did not present diffraction peaks assignable to the metal species. The absence of peaks attributed to the metal species may indicate that the metal species might not be crystalline, but homogeneously and highly dispersed either as single-atoms or nanoparticles smaller than 2 nm [56]. The diffraction peak at 19° observable in some of the treated samples may correspond to structural ordering processes that occur in the carbon material during C_3N_4 synthesis. These structural ordering processes have also been observed in absence of C_3N_4 and metals for heat-treated KUA (Figure S1a). Interestingly, in absence of C_3N_4, some diffraction peaks with low intensity were detected in the diffractograms of Cu/KUA and Fe/KUA that can be related to metal species (Figure S1b), which reveal

Table 1
Yields obtained after carbonisation treatments, nitrogen content determined by elemental analysis (%N (at.%) EA), and metallic content (%M ICP (wt.%)) determined by ICP.

Sample	Yield (%)	%N (at. %) EA	%M ICP (wt. %)
C_3N_4	50	63.0	-
C3N4/KUA_15	85	1.63	-
Fe–C3N4/KUA_15	82	1.34	1.3
Cu–C3N4/KUA_15	83	2.30	1.5
C3N4/KUA_30	74	3.13	-
Fe–C3N4/KUA_30	71	2.41	1.3
Cu–C3N4/KUA_30	75	3.06	1.6
C3N4/KUA_50	63	4.28	-
Fe–C3N4/KUA_50	57	5.50	1.4
Cu–C3N4/KUA_50	61	4.61	1.8

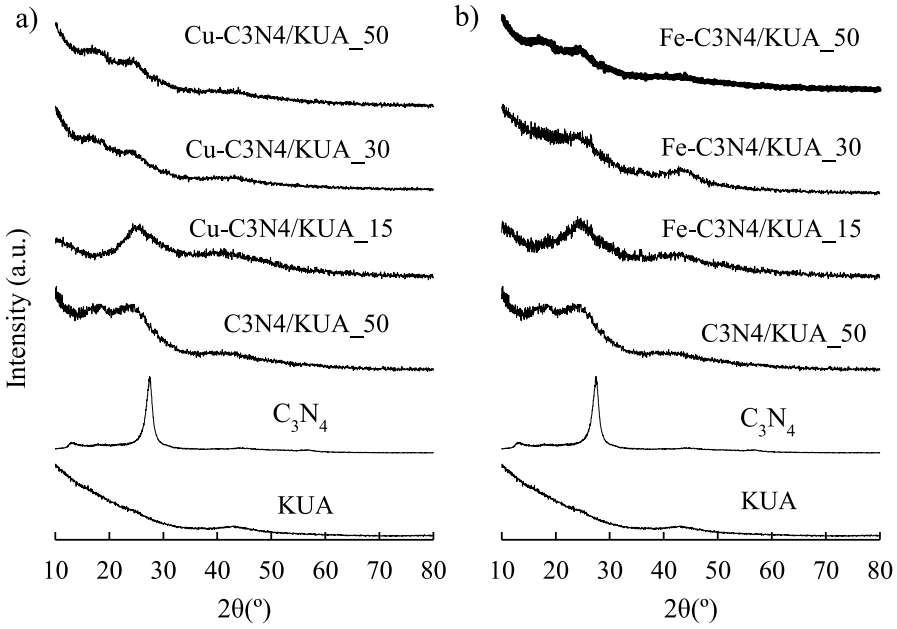

Fig. 1. XRD diffractograms of a) Cu–C3N4/KUA and b) Fe–C3N4/KUA samples. (A colour version of this figure can be viewed online.)

the importance of C_3N_4 to achieve a homogeneous distribution of highly dispersed metal species.

TEM micrographs are included in Fig. 2. Fig. 2a and b show the TEM images of KUA and C3N4/KUA_50 samples, respectively. It can be observed that KUA has a disordered structure characteristic of a highly porous carbon material, which is not modified after the incorporation of C_3N_4, suggesting that C_3N_4 is very well-dispersed in the composite material. Nevertheless, the higher and homogeneous contrast observed in this image suggests that C_3N_4 is homogeneously distributed in the microporosity of the activated carbon. Cu-based electrocatalysts (Fig. 2c, e, and 2g) did not show significant differences compared to the pristine carbon material, indicating that metal nanoparticles detectable by TEM were not formed, which is in good agreement with XRD results. However, TEM images of Cu/KUA sample showed the formation of particles (Figure S2a).

TEM images for Fe–C3N4/KUA electrocatalysts revealed the presence of different structures. Fe–C3N4/KUA_15 (Fig. 2d) displays a very similar morphology to that of metal-free materials. Interestingly, darker regions with spherical or oval shapes and sizes of 10–20 nm and 3–8 nm are observed in the micrographs recorded for Fe–C3N4/KUA_30 (Fig. 2f) and in Fe–C3N4/KUA_50 (Fig. 2h), respectively. Due to the low iron content present in the samples (~1 wt %), such quantity of dark regions observed in those materials cannot be attributed to iron particles, but to the presence of C_3N_4-type domains on KUA. The formation of larger C_3N_4-type nanodomains is favoured by the presence of iron since it has been reported to play an important role as a catalyst for the synthesis of C_3N_4 [26]. Iron atoms coordinate dicyandiamide molecules via the sp^2 nitrogen electron pair and the complex formed plays a crucial role in the formation of the supramolecular C_3N_4, where the single-atom configuration is favoured [26]. It should be noted that those relatively large C_3N_4 domains were detected neither in Fe–C3N4/KUA_15 nor in the Cu-based electrocatalysts, in which C_3N_4 might be in the form of well-dispersed nano-structures. Interestingly, small black dots embedded into the dark C_3N_4 domains can be distinguished in Fe–C3N4/KUA_50 (Fig. 2h), which suggests the presence of species with a very different molecular weight and might be related to the presence of small iron clusters. Moreover, the TEM images of Fe/KUA samples prepared in absence of C_3N_4 showed the formation of nanoparticles (Figure S2b), which are not observed for samples with low C_3N_4 contents.

The textural properties of all materials were studied through N_2-adsorption isotherms. Fig. 3 includes the N_2 adsorption-desorption isotherms (Fig. 3a) and pore size distribution (PSD) (Fig. 3b) of KUA and representative samples. Table 2 summarises the porous texture data of all samples. As can be seen in Fig. 3a, all adsorption isotherms were of type I, being consistent with the microporous character of the materials. The PSD plotted in Fig. 3b showed two main contributions, the first corresponds to the narrowest micropores, centred at 0.8 nm, and the second one corresponds to the widest micropores, centred at 1.8 nm. The samples are mainly microporous, but they also have some mesoporosity between 2 and 4 nm. The micropore volume (V_{micro}) is lower than the total pore volume (V_t) for all the samples (Table 2), showing that the samples also present some mesoporosity.

The results presented in Table 2 show that the BET surface area of the composite material progressively decreases compared to that of the original carbon material (3180 m^2/g) when the amount of C_3N_4 increases in the composite. Nevertheless, it is worth mentioning that the resulting samples still present a very high apparent surface area and micropore volume, even for the larger contents of C_3N_4. The porous texture is well preserved in C3N4/KUA and Cu–C3N4/KUA samples. However, iron samples showed a more marked decrease in the apparent surface area compared to the counterpart metal-free material and the copper-containing equivalent samples for C_3N_4 contents of 30 and 50%. When comparing S_{BET} obtained for the samples with the expected S_{BET} calculated with the mixtures rule, it is clearly observed that some porosity becomes blocked for the higher contents of C_3N_4 when Fe is present (Table 2). In addition, considering the bulk density of C_3N_4 we have estimated the remaining volume of pores of the activated carbon and, from that value, the volume occupied by the C_3N_4 material can be calculated and, for the highest C_3N_4 content, it is around 0.3 cm^3/g. The results suggest that C_3N_4 precursor may have decomposed in the form of nano-domains within the porosity and not as large C_3N_4 sheets, which is in agreement with TEM and XRD results. The presence of Cu leads to small C_3N_4 domains within the porous texture of the materials, similarly to what is observed for C3N4/KUA, while the presence of Fe atoms leads to the formation of larger C_3N_4 domains, which may partially block the porosity and affect more sharply its pristine textural properties. It should be noted that sample Fe–C3N4/KUA_50, in which the presence of C_3N_4 domains was observed in the TEM micrographs (Fig. 2h), displayed the most important decrease of the S_{BET} and volume of micropores

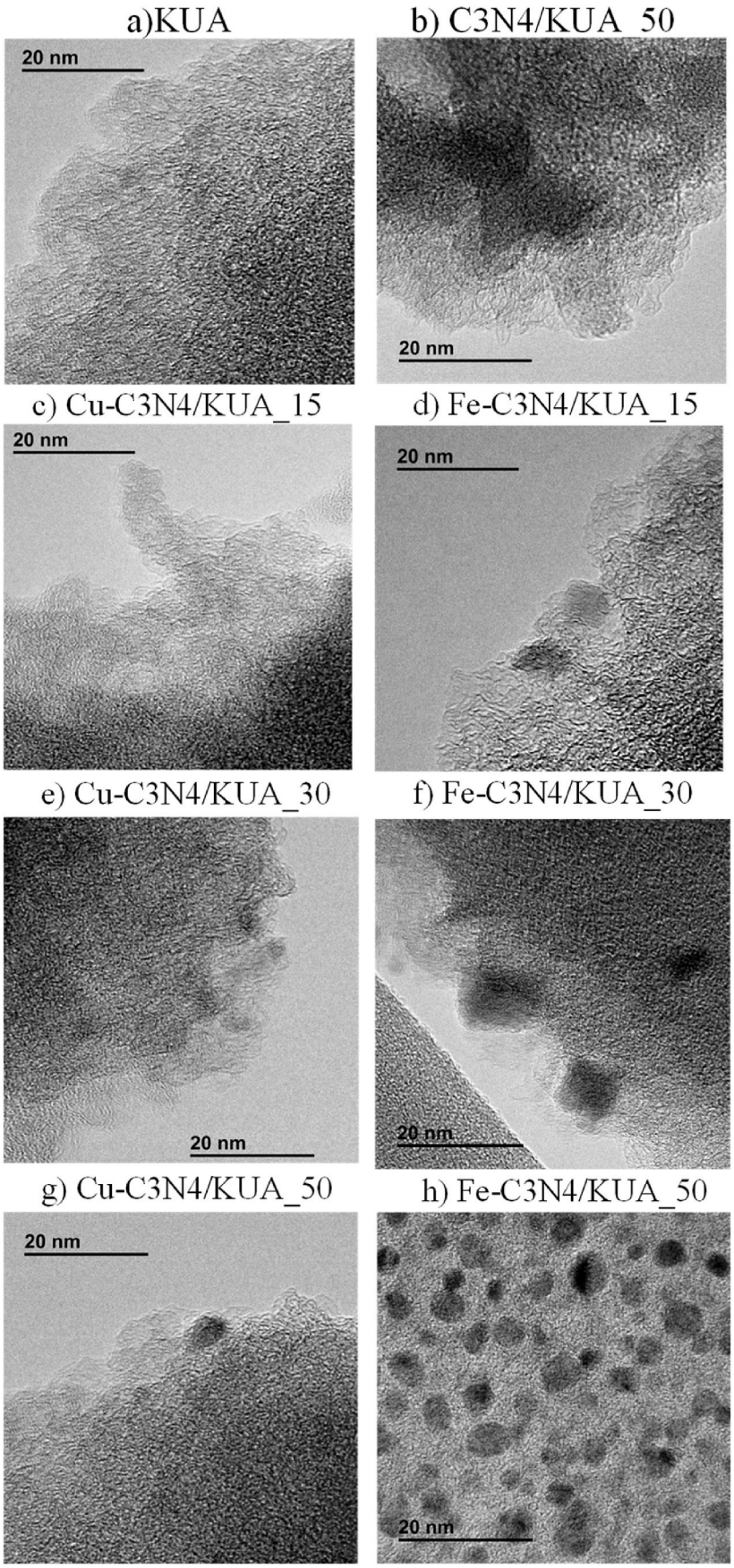

Fig. 2. TEM images of a) KUA b) C3N4/KUA and, c-h) M-C3N4/KUA samples. (A colour version of this figure can be viewed online.)

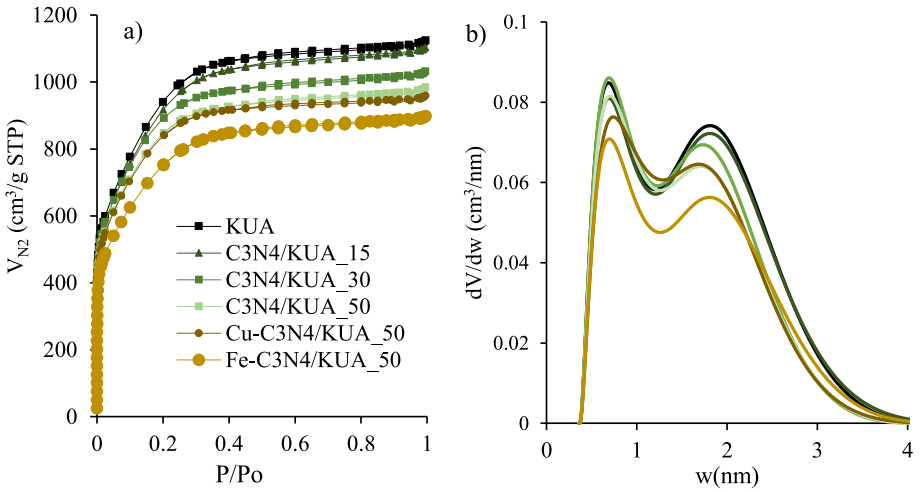

Fig. 3. a) N_2 adsorption-desorption isotherms and b) PSD representations of KUA, C3N4/KUA and M-C3N4/KUA_50 samples. (A colour version of this figure can be viewed online.)

Table 2
Results of the characterisation of the porous texture.

Sample	S_{BET} (m^2/g)	V_{micro} (cm^3/g)	V_t (cm^3/g)	S_{BET} (m^2/g) Mixtures law	$V_{t\ KUA}$ -m_{C3N4}/ρ_{C3N4} (cm^3/g_{KUA})
KUA	3180	1.09	1.64	-	-
C_3N_4	6	-	0.02	-	-
C3N4/KUA_15	3090	1.06	1.56	2960	1.50
Fe–C3N4/KUA_15	3090	1.06	1.57	3030	1.55
Cu–C3N4/KUA_15	2950	1.04	1.47	3000	1.53
C3N4/KUA_30	2970	1.07	1.46	2880	1.45
Fe–C3N4/KUA_30	2730	1.01	1.34	2950	1.50
Cu–C3N4/KUA_30	2800	1.10	1.36	2830	1.41
C3N4/KUA_50	2810	1.02	1.39	2640	1.29
Fe–C3N4/KUA_50	2310	0.87	1.27	2820	1.41
Cu–C3N4/KUA_50	2670	1.01	1.32	2690	1.32

compared to the pristine KUA sample.

The surface chemistry of the materials was characterised by XPS. Concerning individual spectra, N 1s were registered for M-C3N4/KUA samples and pure C_3N_4 (Fig. 4). According to previous studies, N 1s spectra for C_3N_4 can be deconvoluted into three peaks [54,57]. The first peak (~398.6 eV) corresponds to sp^2 nitrogen atoms (-C═N–C-) that are present in triazine and heptazine rings that compose the C_3N_4 structure, the second peak (~399.8 eV) can be assigned to nitrogen atoms bonding the heptazine rings (N–C_3) and amine terminal groups (-NH_2), and the third peak (~401.0 eV) peak corresponds to quaternary nitrogen atoms or nitrogen atoms positively charged, which usually appear in N 1s spectra as a consequence of the X-ray irradiation during the measurement. The N 1s spectra of C3N4/KUA samples confirmed the successful formation of C_3N_4 domains in the composite.

As can be seen in Fig. 4 and Table 3, N 1s XPS spectra registered for the as-synthesized C_3N_4 and composite materials presented the same three contributions centred at equivalent binding energies to bare C_3N_4. However, some differences can be observed, especially in the peak located at ~399.8 eV. This contribution significantly increases from 24% in pure C_3N_4 to >30% in the rest of the samples, being this increase more important in the materials in which metals are introduced and with the lower C_3N_4 contents (Table 3). It has been reported that the presence of M-N_x single atoms produces a contribution at ~399.5 eV [34], so the large relative contribution of the peak at ~399.8 eV in these samples suggests the presence of M-N_x species in the resulting materials. Finally, the 401.0 eV peak is almost constant in all C3N4/KUA and M-C3N4/KUA samples, but the relative contribution is significantly higher than the observed for C_3N_4, so the formation of quaternary nitrogen species, which present this same binding energy, can not be ruled out.

Fig. 5 contains the Cu and Fe 2p XPS for the different catalysts. In Cu–C3N4/KUA samples, the peak corresponding to $2p_{3/2}$ transition in Cu 2p spectra can be deconvoluted into two contributions: the first peak (932.8 eV) that corresponds to Cu^+ and the second contribution at 934.7 eV, which is often assigned to Cu^{2+} [58–60]. The ratio between Cu^+ and Cu^{2+} is presented in Table 3. In Fe–C3N4_KUA samples (Fig. 5b), the Fe 2p spectra show a contribution associated with the presence of Fe^{3+}. The $2p_{3/2}$ peak can be deconvoluted with a multiplet of 4 peaks with binding energies of 709.8, 710.7, 711.4, and 712.3 eV and the contribution at 715 eV which corresponds to the satellite peak [61]. The absence of Fe^{2+} (binding energies at 709.6 eV and 53.7 eV for 2p and 3p regions, respectively) and Fe^0 (binding energies at 706.7 and 53.0 eV for 2p and 3p regions, respectively) was checked in 2p and 3p spectra (Fig. 5 and Figure S3), respectively, for all the samples. While iron maintains the oxidation state of the metal precursor ($Fe(NO_3)_3$), copper suffered reduction processes during the synthesis in presence of carbon material. This fact is coherent with copper and iron Ellingham diagrams [62]. The comparison between the total and surface concentration of metals (ICP and XPS, respectively) showed that both metals are preferentially located on the surface. The amount of surface metal detected by XPS is lower for higher amounts of C_3N_4. That result may indicate that the excess of C_3N_4 is somehow shielding the metal species, which is more notorious in the case of Fe–C3N4/KUA electrocatalysts.

3.2. Electrochemical characterisation

The voltammograms obtained are plotted in Figure S4. As can be observed, all samples showed the typical rectangular profile of porous carbon materials. M-C3N4/KUA samples presented more rectangular profiles than the original KUA. This is associated with the improvement

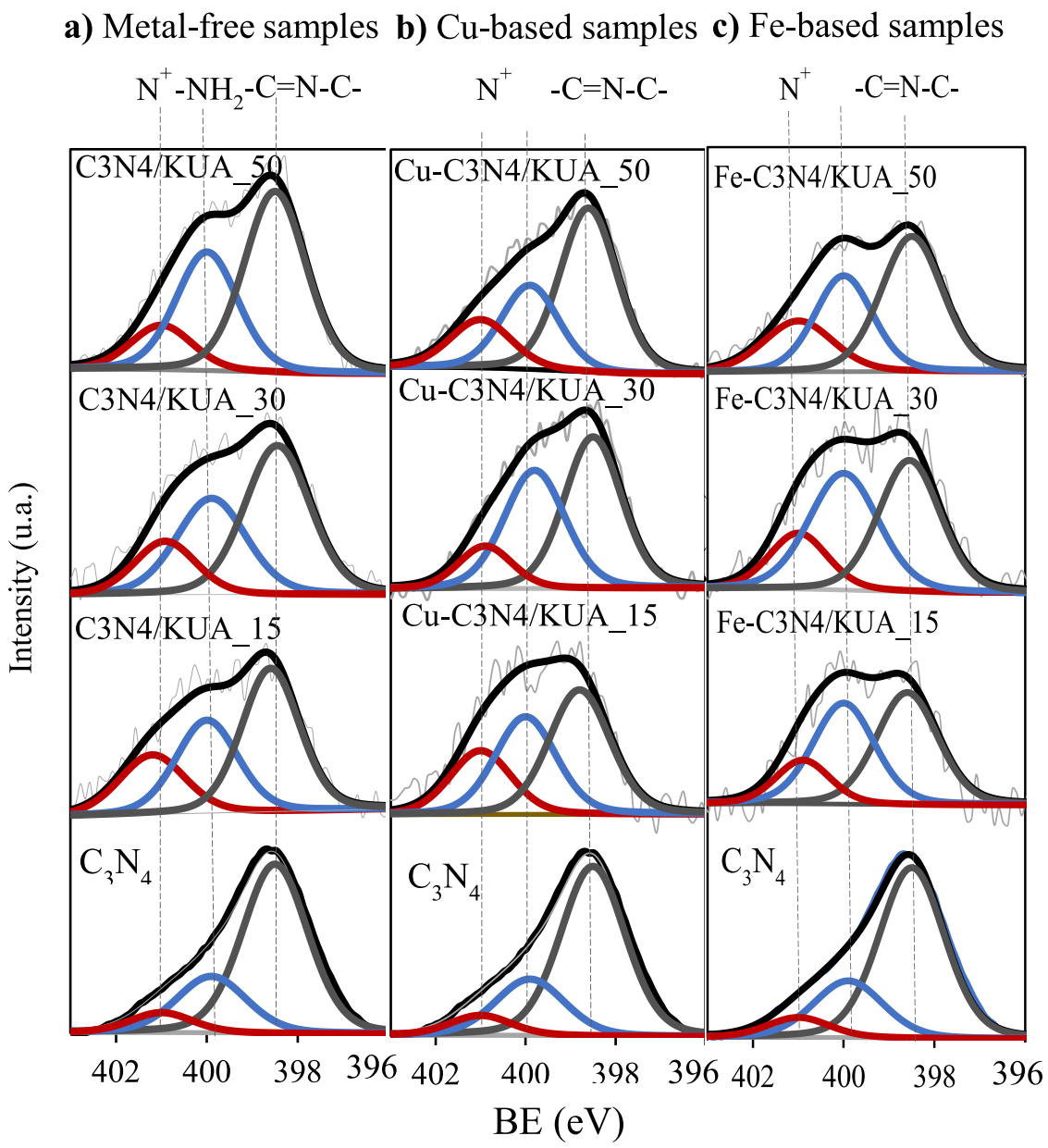

Fig. 4. N 1s XPS spectra of a) C3N4/KUA_XX, b) Cu–C3N4/KUA_XX, and c) Fe–C3N4/KUA_XX. (A colour version of this figure can be viewed online.)

in the electrical conductivity of the samples due to the presence of C_3N_4, which is a well-known material that possesses high electrical conductivity [63] or due to the presence of M−N sites [64]. In the case of Cu–C3N4/KUA electrocatalysts, faradaic processes were observed at around 0.6 V, which can be related to Cu^{2+}/Cu^{+} redox processes, and the reduction process to Cu^0 was not observed. Cu SACs can present such Cu^{2+}/Cu^{+} potential-driven evolution, where Cu^{+} is stabilized by the local structure and Cu^0 is usually not observed [65], while CuO nanoparticles present redox processes at different potentials [66]. The charge corresponding to these redox processes are related with the electrochemically active surface copper against the total amount of Cu, which decreases from Cu–C3N4/KUA_15 to Cu–C3N4/KUA_50. However, the large value of double layer introduces high error in the determination of the electrochemically active Cu. Nevertheless, these results are in agreement with the decrease in electrocatalytic activity. No faradaic processes could be observed for Fe–C3N4/KUA samples in the potential range studied, as it has been reported for other Fe–N–C catalysts [67]. The specific capacitance for M-C3N4/KUA_15 decreases slightly compared to KUA, which is in agreement with the change in porosity of the materials (Table 2 and Table S1). However, this decrease in capacitance is much more important for 30 and 50% C_3N_4-containing materials compared to the measured porosity, which suggests the existence of important differences in the interaction with the electrolyte (Table 2 and Table S1).

The electrocatalytic properties of all prepared materials and reference samples were studied through LSV experiments in an O_2-saturated 0.1 M KOH solution (see Fig. 6). As the indicators of the catalytic activity, onset potential for the reaction (E_{onset}), half-wave potential ($E_{1/2}$), the number of electrons transferred calculated (n_{KL}) and the percentage of H_2O_2 (% H_2O_2) are shown in Table 4. The synergistic effect of Fe and Cu dispersed species embedded into the C_3N_4 nano-domains can be clearly seen in Fig. 6a and b. For the comparison of the studied materials with benchmark electrocatalysts (KUA, C3N4/KUA_15 and the commercial electrode Pt/C), LSV curves of the best metal-containing C3N4/KUA catalysts are shown in Fig. 6c.

The C_3N_4-free samples (Cu/KUA and Fe/KUA) displayed poorer

Table 3
Main parameters obtained from N 1s and M 2p XPS spectra.

Sample	% -C═N–C-	% N–C_3/NH_2/M-N_x	% –N^+	Cu^+/Cu^{2+}	%M XPS (wt. %)[a]
C_3N_4	68	24	8	-	-
C3N4/KUA_15	46	32	22	-	-
C3N4/KUA_30	49	34	17		
C3N4/KUA_50	53	34	13		
Cu–C3N4/KUA_15	44	34	22	2.0	2.8
Cu–C3N4/KUA_30	48	40	12	2.2	2.3
Cu–C3N4/KUA_50	55	29	16	2.0	1.9
Fe–C3N4/KUA_15	45	40	15	-	3.6
Fe–C3N4/KUA_30	46	30	24		1.6
Fe–C3N4/KUA_50	48	32	20		1.3

[a] Surface metal content calculated from XPS atomic percentage.

catalytic properties compared to pristine KUA, which demonstrates the high catalytic activity of this highly porous material. As can be observed, Cu–C3N4/KUA and Fe–C3N4/KUA electrocatalysts had an onset potential higher than 0.85 V, which is higher than that of pristine carbon material (0.82 V). Among Fe–C3N4/KUA samples, Fe–C3N4/KUA_15 shows an outstanding selectivity to the 4-electron-pathway (n_{KL} of 3.5), while the number of electrons transferred decreases for the samples with higher C_3N_4 contents (n_{KL} of 2.7 and 2.0 for Fe–C3N4/KUA_30 and Fe–C3N4/KUA_50, respectively). Such a tendency may be related to the partial blockage or some micropore filling of the carbon material porosity for those samples with larger C_3N_4 contents, in which part of the active sites become inaccessible, as well as to the lower content of surface Fe sites observed in Fe–C3N4/KUA_30 and Fe–C3N4/KUA_50 according to XPS results. In the case of Cu–C3N4/KUA samples, the best selectivity towards the 4-electron-pathway was also presented by the electrocatalysts with the lowest C_3N_4 content (n_{KL} of 3.6), and a similar tendency to that seen for the Fe–C3N4/KUA samples was observed, but the effect of the C_3N_4 content is less pronounced, which is in agreement with the less marked decrease of surface metal sites in Cu–C3N4/KUA_30 and Cu–C3N4/KUA_50 (versus Cu–C3N4/KUA_15) compared to the Fe-containing counterpart electrocatalysts (see Table 3). These better results achieved by Cu–C3N4/KUA electrocatalysts may be related to the better dispersion of Cu species in the samples associated with the presence of C_3N_4-type nano-domains able to stabilize the copper species by affording multiple anchorage sites.

Among the studied samples, Cu–C3N4/KUA_15 electrocatalyst displayed the best catalytic behaviour in terms of current density, the number of electrons transferred, and especially $E_{1/2}$. Regarding the similarities observed in the structural characterisation of Cu–C3N4/KUA_15 and Fe–C3N4/KUA_15, the perceptible differences observed in selectivity and $E_{1/2}$ (Table 4) might be originated from intrinsic distinct catalytic activities of copper and iron sites.

Moreover, the high micropore volume of the activated carbon is an additional beneficial factor contributing to the outstanding activity of the Cu and Fe containing materials in which the lowest C_3N_4 content has been incorporated. As observed for KUA (Fig. 6c), micropores themselves can act as nanoreactors for the ORR favouring an increase in O_2 concentration [68,69].

In order to check whether the oxygen functional groups present in the carbon material affect the activity of the samples towards ORR, the catalytic activity of Cu–C3N4/KUA_15 and the counterpart material prepared with KUA heat-treated at 900 °C (Cu–C3N4/KUA(900)_15) are compared in Figure S5. These results indicate that oxygen functional groups are not affecting significantly the C_3N_4 synthesis and a similar

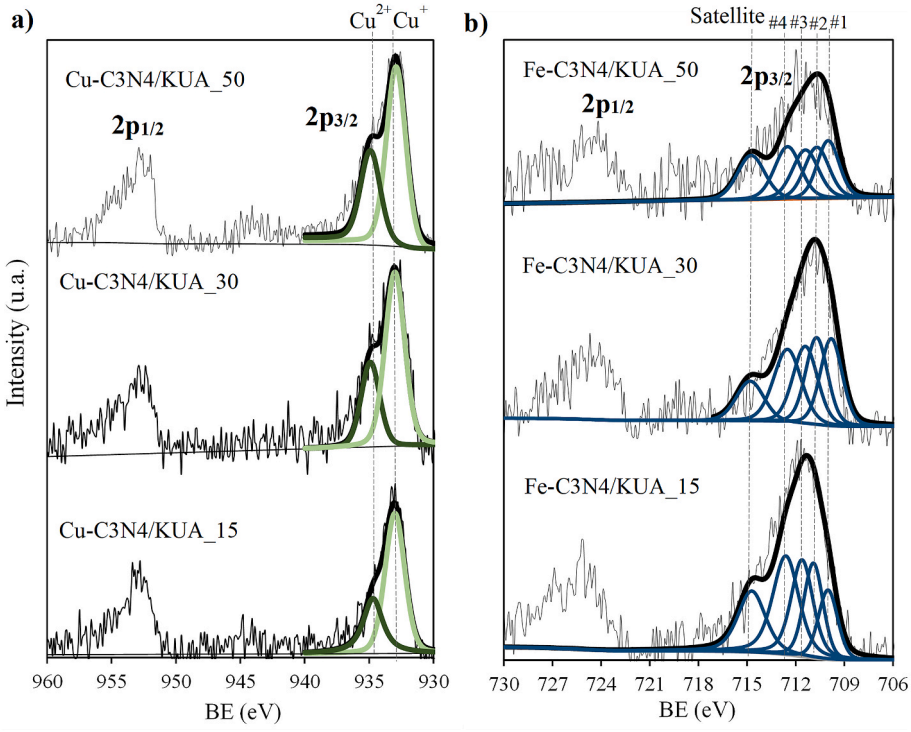

Fig. 5. 2p XPS spectra of a) Cu–C3N4/KUA and b) Fe–C3N4/KUA samples. (A colour version of this figure can be viewed online.)

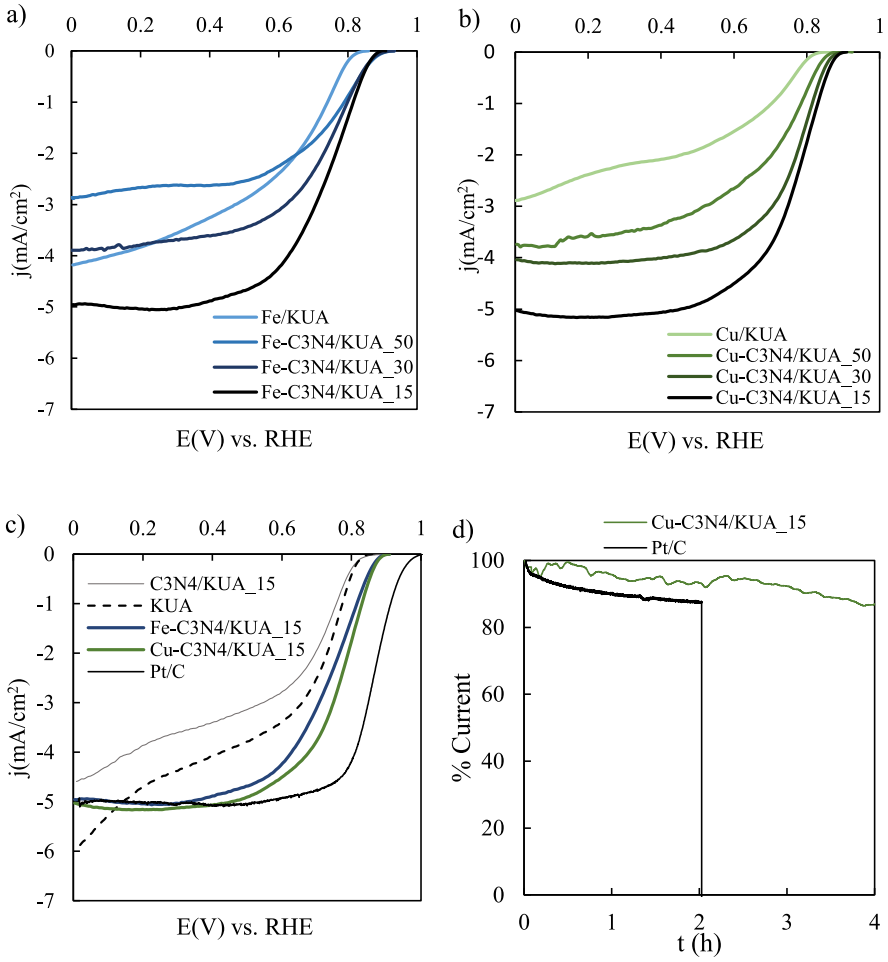

Fig. 6. LSV curves for (a) Fe–C3N4/KUA and (b) Cu–C3N4/KUA samples at 5 mV/s and 1600 rpm in an O_2-saturated 0.1 M KOH solution. (c) Comparison of LSV curves of the best performing samples and the reference materials. (d) Chronoamperometric experiments for the best performing sample (Cu–C3N4/KUA_15) and the commercial Pt-based electrode at a fixed potential of 0.65 V. After 2 h of experiment, methanol was added into the solution up to a concentration of 1 M. (A colour version of this figure can be viewed online.)

Table 4
Parameters obtained from LSV curves (O_2, 1600 rpm, 0.1 M KOH).

Sample	E_{onset} (V) −0.1 mA cm^{-2}/ Tangent method	$E_{1/2}$ (V)	n_{KL}	% H_2O_2
KUA	0.82/0.82	0.67	2.6	70
Cu–C3N4/KUA_15	0.88/0.87	0.78	3.6	20
Cu–C3N4/KUA_30	0.87/0.86	0.77	2.9	55
Cu–C3N4/KUA_50	0.85/0.85	0.71	2.6	70
Fe–C3N4/KUA_15	0.87/0.87	0.74	3.5	25
Fe–C3N4/KUA_30	0.88/0.87	0.71	2.7	65
Fe–C3N4/KUA_50	0.88/0.88	0.71	2.0	100
Pt/C	0.97/0.94	0.86	3.8	10
Cu/KUA	0.81/0.81	0.60	2.0	100
Fe/KUA	0.81/0.81	0.62	2.9	55

electrochemical activity is obtained.

In addition, the catalytic activity of a sample C3N4/KUA_15 without metal was measured (Fig. 6c) and the catalytic activity is even lower than that of pristine KUA sample. Then, the contribution of the N groups formed in the carbon material seems not to be responsible for the observed electrochemical activity improvement when metal is present. In addition, the increase in the amount of C_3N_4 precursor does not result in higher catalytic activities. This means that the N species in the C_3N_4, or formed by reaction with the activated carbon, do not act as active sites towards the ORR.

Therefore, the composite materials with a high dispersion of both C_3N_4 and metal sites with the lowest decrease in micropore volume are those with the highest electrocatalytic activity, being the catalyst Cu–C3N4/KUA_15, where the micropore volume is the less modified after the incorporation of C_3N_4 and Cu, the one exhibiting the highest performance.

Chronoamperometric experiments were performed to measure the stability and the resistance against methanol poisoning of the best electrocatalytic material, Cu–C3N4/KUA_15, and the same experiment was also carried out for the commercial Pt/C electrocatalyst for comparison purposes (Fig. 6d). The chronoamperometry assay showed that, after 2 h of reaction, Cu–C3N4/KUA_15 showed a retention of the catalytic activity (93.4%) that was superior to the obtained from the commercial Pt-based electrode (87.5%), pointing out the excellent properties of Cu–C3N4/KUA_15 material as electrocatalyst towards ORR. Then, methanol was added until 1 M concentration in order to study the resistance against methanol poisoning. In Pt/C electrode, the methanol addition caused a rapid poisoning and the current density decreased to zero, while Cu–C3N4/KUA_15 electrocatalyst displayed a high resistance against methanol poisoning. The stability shown by Cu–C3N4/KUA_15 electrocatalyst may be related to the presence of M-N_x species, which are known to present superior stability to metal nanoparticles since metal species are anchored to four nitrogen atoms that create strong bonds and a very stable conformation for metal disposition [8]. Figure S6 shows the chronoamperometric experiments of KUA and Cu–C3N4/KUA_15 samples where the currents of KUA and Cu–C3N4/KUA_15 in the chronoamperometry measurement are compared to evaluate their stability. As it can be observed, the current is around three times higher for sample Cu–C3N4/KUA_15, thus demonstrating that the electrocatalytic activity, and the observed stability, are due to the M-C3N4 species.

To check the effect of metal leaching, we have performed a leaching experiment in the conditions used experimentally (0.1 M KOH solution) for the time of the stability test (4 h) for the best performing samples (Cu–C3N4/KUA_15 and Fe–C3N4/KUA_15). While in the iron-containing sample the leaching observed was negligible, the copper sample lost 33% of the metal content. Since the electrocatalytic activity retained after 4 h was still 87%, part of the leached metal might correspond to weakly anchored Cu which did are not bonded through Cu–N interactions and that do not contribute significantly to the catalytic activity. XPS N 1s spectra of the samples after the leaching test (Figure S7) did not show important modifications with respect to the initial catalysts, suggesting that the C3N4-type nanodomains were not significantly affected by the reaction conditions.

3.3. Computational calculations

The initial M-C3N4 flakes were optimised resulting in different conformations (See Fig. 7). According to the calculations, the lower-energy conformation for Cu–C3N4 flake was Cu–N_2 (Fig. 7a), while in Fe–C3N4 flakes the Fe central atom was bonded to 4 nitrogen atoms (Fe–N_4, Fig. 7b). This difference in the coordination of the metal is in good agreement with the results found by other authors [18,70].

Prior to the evaluation of the catalytic activities, Pourbaix diagrams were calculated for Cu–C3N4 and Fe–C3N4 flakes (Figure S8). According to the diagrams, the most stable species for both systems in the potential range studied (0–1 V) is the M-OH. Since C_3N_4 was synthesized on the pore walls of the carbon material, one side of the C_3N_4 flake is sterically hindered. Therefore, considering MOH-C3N4 as the initial species, the release of the metal sites that participate in the ORR catalytic cycle, firstly requires the reduction of the M-OH. After that, the ORR process occurs as illustrated in Scheme 2. This scheme shows the proposed ORR mechanism for Cu–C3N4 flakes after the M−OH reduction. The key step is the reduction of OOH* intermediates (step 3 to 4 in Scheme 2), in which two possible pathways could take place. The red arrow corresponds to the formation of hydrogen peroxide, corresponding to the 2-electrons pathway, and the blue path corresponds to the 4-electron-pathway, leading to two water molecules. The counterpart reaction mechanism for Fe–C3N4 is shown in Scheme S1.

Fig. 8 shows the free-energy diagrams for both M-C3N4 flakes applying a moderate overpotential (E = 0.80 V). The diagrams show that the 4-electron pathway is more energetically demanding in the case of the iron system, being the stability of FeOH–C3N4 species the aspect that may determine its lower catalytic activity compared to Cu-containing catalysts. The free-energies calculated at E = 0.80 V for the MOH-C3N4 to M-C3N4 reduction (step 5 to 1 in Scheme 2) are significantly lower for Cu (1.47 eV) than for Fe (2.14 eV) flakes. Interestingly, the higher reduction energies calculated for FeOH–C3N4 are coherent with the lower $E_{1/2}$ values observed experimentally (Table 4). Besides, the formation of hydrogen peroxide is energetically more inaccessible in the case of Cu–C3N4 than for Fe–C3N4 at any potential studied. Therefore, Cu–C3N4 flakes show a theoretical superior catalytic behaviour towards the ORR, including selectivity and activity. Here, computational calculations indicate that, besides the structural differences between copper and iron-containing materials observed in the present work, the better catalytic properties displayed by Cu–C3N4/KUA may also be originated from an intrinsic superior catalytic behaviour of Cu–C3N4 sites. Interestingly, for M-C3N4/KUA_15 samples (with low C_3N_4 content and in which the structural differences are minimal), slight differences in n_{KL} and important $E_{1/2}$ differences were observed (Table 4), both supported by the information obtained from computational calculations.

Interestingly, there are some differences between these results and those observed in some other studies reported in the literature and our previous results with metal phthalocyanines (Pc) [14,71–73]. We believe that this different behaviour in the experimental results, and also in DFT calculations, is strongly related to the C_3N_4 that is used as the anchoring point for the metal active sites. C_3N_4 is a well-known material that possesses unusual features, as it exhibits high electrical conductivity and may induce electron delocalization in the materials. This might produce changes in the electron density of the metal active sites, which in turn may result in different ORR catalytic activity from those reported for other electrocatalysts like those based on Pc.

4. Conclusions

A series of copper and iron-based electrocatalysts have been prepared on C_3N_4/KUA composites with various carbon nitride contents by following a straightforward and reproducible synthetic protocol. The characterisation of the materials led to a deep understanding of the differences between Cu and Fe-based electrocatalysts. It was observed that the presence of iron generated higher C_3N_4 domains as a consequence of the strong coordination of C_3N_4 precursor and metal during the synthesis, while Cu-containing counterparts presented well-distributed C_3N_4-type nano-domains and highly dispersed metal species. According to the similarities observed for Cu–C3N4/KUA and C3N4/KUA samples, copper may have essentially an inert role in the synthesis of carbon nitride.

Samples with moderate C_3N_4 content (15% of precursor) perform better for the ORR as they present the maximum amount of both surface metal active sites and available microporosity. The stability test performed with the most interesting sample, Cu–C3N4/KUA_15, showed that the electrocatalyst had good stability and high resistance to methanol poisoning. The computational DFT calculations suggest that

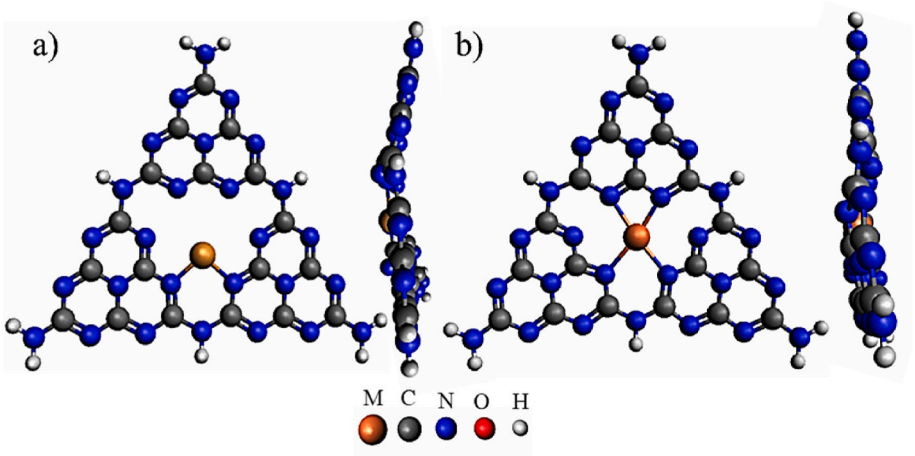

Fig. 7. a) Cu–C3N4 and b) Fe–C3N4 optimised structures used for the DFT calculations. (A colour version of this figure can be viewed online.)

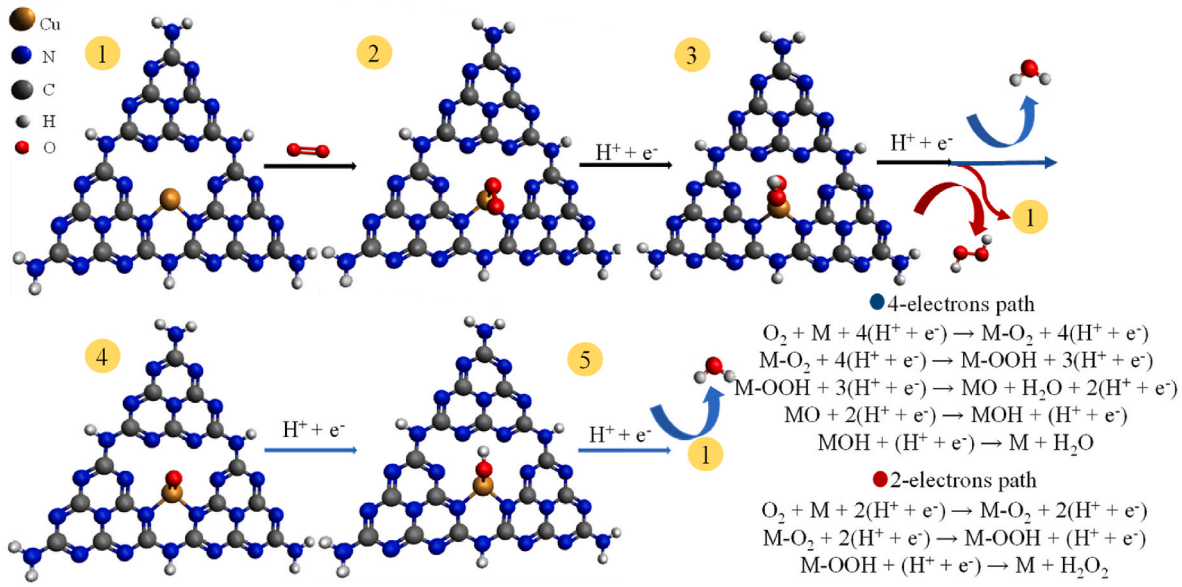

Scheme 2. ORR catalytic cycle scheme for Cu–C3N4.

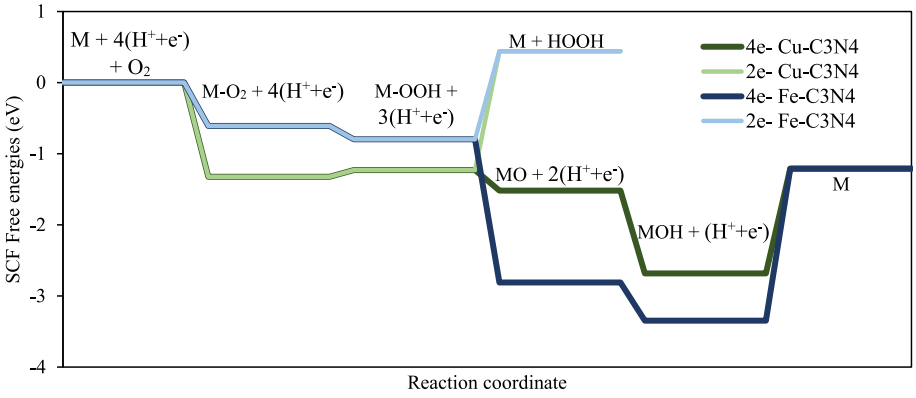

Fig. 8. ORR free-energy diagrams (E = 0.80 V) for 4-electrons and 2-electrons pathways. (A colour version of this figure can be viewed online.)

Cu–C3N4 sites have superior catalytic properties than Fe–C3N4, both for activity and selectivity, being consistent with the experimental results.

These materials, with highly dispersed transition metals strongly bonded to well-distributed C_3N_4-type nanodomains on the pore walls of a high micropore volume carbon support, have an outstanding performance due to the beneficial contribution of both metal active sites and micropores. These catalysts are much more cost-effective than commercial Pt-based electrocatalysts and they still have a wide room for improvement taking into account the possibility of studying other metals using computational calculations as a predictive tool and post-synthesis treatments.

CRediT authorship contribution statement

G. Alemany-Molina: Data curation, Formal analysis, Investigation, Writing – original draft. **J. Quílez-Bermejo:** Data curation, Formal analysis, Writing – original draft. **M. Navlani-García:** Formal analysis, Investigation, Writing – review & editing, Funding acquisition. **E. Morallón:** Conceptualization, Investigation, Methodology, Supervision, Writing – review & editing. **D. Cazorla-Amorós:** Conceptualization, Investigation, Methodology, Supervision, Writing – review & editing, Funding acquisition, Project administration.

Declaration of competing interest

The authors declare the following financial interests/personal relationships which may be considered as potential competing interests: Diego Cazorla-Amorós reports financial support was provided by Spain Ministry of Science and Innovation. Diego Cazorla-Amorós reports financial support was provided by European Regional Development Fund. Miriam Navlani-García reports financial support was provided by Valencia Directorate of Research Culture and Sport. Gabriel Alemany-Molina reports financial support was provided by Spain Ministry of Universities. Prof. Emilia Morallón is acting as Editor of the Carbon Journal.

Acknowledgements

This work was financed by the MCI/AEI/FEDER, UE (RTI2018-095291-B-I00). G.A.M thanks the Research Initiation Scholarship from Vicerrectorado de Investigación y Transferencia de Conocimiento of the University of Alicante and Ministerio de Universidades (grant number: FPU20/03969). M.N.G. thanks the Plan GenT project (CDEIGENT/2018/027) for the financial support.

Appendix A. Supplementary data

Supplementary data to this article can be found online at https://doi.org/10.1016/j.carbon.2022.05.003.

References

[1] United Nations Framework Convention on Climate Change, Paris agreement (Annex to decision 1/CP.21, document FCCC/CP/201510/Add.1 Paris: United Nations, Retrieved from, http://unfccc.int/resource/docs/2015/cop21/eng/10a01.pdf, 2015.

[2] W. Zappa, M. Junginger, M. Van den Broek, Is a 100% renewable European power system feasible by 2050? Appl. Energy 233 (2019) 1027–1050, https://doi.org/10.1016/j.apenergy.2018.08.109.

[3] L.M. Gandía, G. Arzamendi, P.M. Diéguez, Renewable hydrogen energy: an overview, in: L.M. Gandía, G. Arzamendi, P.M. Diéguez (Eds.), Renewable Hydrogen Technologies: Production, Purification, Storage, Applications and Safety, Elsevier, Amsterdam, 2013, pp. 1–18.

[4] C. Song, Fuel processing for low-temperature and high-temperature fuel cells: challenges, and opportunities for sustainable development in the 21st century, Catal. Today 77 (1–2) (2002) 17–49, https://doi.org/10.1016/S0920-5861(02)00231-6.

[5] H.A. Gasteiger, J.E. Panels, S.G. Yan, Dependence of PEM fuel cell performance on catalyst loading, J. Power Sources 127 (1–2) (2004) 162–171, https://doi.org/10.1016/j.jpowsour.2003.09.013.

[6] C. Sealy, The problem with platinum, Mater. Today 11 (12) (2008) 65–68, https://doi.org/10.1016/S1369-7021(08)70254-2.

[7] S.H. Talib, Z. Lu, X. Yu, K. Ahmad, B. Bashir, Z. Yang, J. Li, Theoretical inspection of M1/PMA single-atom electrocatalyst: ultra-high performance for water splitting (HER/OER) and oxygen reduction reactions (OER), ACS Catal. 11 (14) (2021) 8929–8941, https://doi.org/10.1021/acscatal.1c01294.

[8] S.K. Kaiser, Z. Chen, D. Faust Akl, S. Mitchell, J. Pérez-Ramírez, Single-atom catalysts across the periodic table, Chem. Rev. 120 (21) (2020) 11703–11809, https://doi.org/10.1021/acs.chemrev.0c00576.

[9] T. Sharifi, E. Gracia-Espino, A. Chen, G. Hu, T. Wågberg, Oxygen reduction reactions on single- or few-atom discrete active sites for heterogeneous catalysis, Adv. Energy Mater. 10 (11) (2020) 1902084, https://doi.org/10.1002/aenm.201902084.

[10] X.X. Wang, D.A. Cullen, Y.T. Pan, S. Hwang, M. Wang, Z. Feng, J. Wang, M. H. Engelhard, H. Zhang, Y. He, Y. Shao, D. Su, K.L. More, J.S. Spendelow, G. Wu, Nitrogen-coordinated single cobalt atom catalysts for oxygen reduction in proton exchange membrane fuel cells, Adv. Mater. 30 (11) (2018) 1–11, https://doi.org/10.1002/adma.201706758.

[11] P. Yin, T. Yao, Y. Wu, L. Zheng, Y. Lin, W. Liu, H. Ju, J. Zhu, X. Hong, Z. Deng, G. Zhou, S. Wei, Y. Li, Single cobalt atoms with precise N-coordination as superior oxygen reduction reaction catalysts, Angew. Chem. Int. Ed. 55 (36) (2016) 10800–10805, https://doi.org/10.1002/anie.201604802.

[12] P. Chen, T. Zhou, L. Xing, K. Xu, Y. Tong, H. Xie, L. Zhang, W. Yan, W. Chu, C. Wu, Y. Xie, Atomically dispersed iron–nitrogen species as electrocatalysts for bifunctional oxygen evolution and reduction reactions, Angew. Chem. Int. Ed. 56 (2) (2017) 610–614, https://doi.org/10.1002/anie.201610119.

[13] Y. Chen, S. Ji, Y. Wang, J. Dong, W. Chen, Z. Li, R. Shen, L. Zheng, Z. Zhuang, D. Wang, Y. Li, Isolated single iron atoms anchored on N-doped porous carbon as an efficient electrocatalyst for the oxygen reduction reaction, Angew. Chem. Int. Ed. 56 (24) (2017) 6937–6941, https://doi.org/10.1002/anie.201702473.

[14] C. González-Gaitán, R. Ruiz-Rosas, E. Morallón, D. Cazorla-Amorós, Relevance of the interaction between the M-phthalocyanines and carbon nanotubes in the electroactivity toward ORR, Langmuir 33 (43) (2017) 11945–11955, https://doi.org/10.1021/acs.langmuir.7b02579.

[15] J.D. Yi, R. Xu, Q. Wu, T. Zhang, K.T. Zang, J. Luo, Y.L. Liang, Y.B. Huang, R. Cao, Atomically dispersed iron-nitrogen active sites within porphyrinic triazine-based frameworks for oxygen reduction reaction in both alkaline and acidic media, ACS Energy Lett. 3 (4) (2018) 883–889, https://doi.org/10.1021/acsenergylett.8b00245.

[16] T. Yoshii, K. Chida, H. Nishihara, F. Tani, Ordered carbonaceous frameworks: a new class of carbon materials with molecular-level design, Chem. Commun. 58 (22) (2022) 3578–3590, https://doi.org/10.1039/d1cc07228e.

[17] S. Fu, C. Zhu, D. Su, J. Song, S. Yao, S. Feng, M.H. Engelhard, D. Du, Y. Lin, Porous carbon-hosted atomically dispersed iron–nitrogen moiety as enhanced electrocatalysts for oxygen reduction reaction in a wide range of pH, Small 14 (12) (2018) 1–7, https://doi.org/10.1002/smll.201703118.

[18] X. Wan, X. Liu, Y. Li, R. Yu, L. Zheng, W. Yan, H. Wang, M. Xu, J. Shui, Fe–N–C electrocatalyst with dense active sites and efficient mass transport for high-performance proton exchange membrane fuel cells, Nat. Catal. 2 (3) (2019) 259–268, https://doi.org/10.1038/s41929-019-0237-3.

[19] L. Jiao, G. Wan, R. Zhang, H. Zhou, S.H. Yu, H.L. Jiang, From metal–organic frameworks to single-atom Fe implanted N-doped porous carbons: efficient oxygen reduction in both alkaline and acidic media, Angew. Chem. Int. Ed. 57 (28) (2018) 8525–8529, https://doi.org/10.1002/anie.201803262.

[20] F. Li, G.F. Han, H.J. Noh, S.J. Kim, Y. Lu, H.Y. Jeong, Z. Fu, J.B. Baek, Boosting oxygen reduction catalysis with abundant copper single atom active sites, Energy Environ. Sci. 11 (8) (2018) 2263–2269, https://doi.org/10.1039/c8ee01169a.

[21] L. Bai, C. Hou, X. Wen, J. Guan, Catalysis of oxygen reduction reaction on atomically dispersed copper- and nitrogen-codoped graphene, ACS Appl. Energy Mater. 2 (7) (2019) 4755–4762, https://doi.org/10.1021/acsaem.9b00386.

[22] L. Cui, L. Cui, Z. Li, J. Zhang, H. Wang, S. Lu, Y. Xiang, A copper single-atom catalyst towards efficient and durable oxygen reduction for fuel cells, J. Mater. Chem. A. 7 (28) (2019) 16690–16695, https://doi.org/10.1039/c9ta03518d.

[23] D. Wang, C. Ao, X. Liu, S. Fang, Y. Lin, W. Liu, W. Zhang, X. Zheng, L. Zhang, T. Yao, Coordination-engineered Cu-N_x single-site catalyst for enhancing oxygen reduction reaction, ACS Appl. Energy Mater. 2 (9) (2019) 6497–6504, https://doi.org/10.1021/acsaem.9b01066.

[24] G. Han, Y. Zheng, X. Zhang, Z. Wang, Y. Gong, C. Du, M.N. Banis, Y.M. Yiu, T. K. Sham, L. Gu, et al., High loading single-atom Cu dispersed on graphene for efficient oxygen reduction reaction, Nano Energy 66 (2019) 2211–2220, https://doi.org/10.1016/j.nanoen.2019.104088.

[25] Y. Zheng, Y. Jiao, Y. Zhu, Q. Cai, A. Vasileff, L.H. Li, Y. Han, Y. Chen, S.Z. Qiao, Molecule-level g-C_3N_4 coordinated transition metals as a new class of electrocatalysts for oxygen electrode reactions, J. Am. Chem. Soc. 139 (9) (2017) 3336–3339, https://doi.org/10.1021/jacs.6b13100.

[26] W. Zhang, Q. Peng, L. Shi, Q. Yao, X. Wang, A. Yu, Z. Chen, Y. Fu, Merging single-atom-dispersed iron and graphitic carbon nitride to a joint electronic system for high-efficiency photocatalytic hydrogen evolution, Small 15 (50) (2019) 1–8, https://doi.org/10.1002/smll.201905166.

[27] Y. Xue, B. Huang, Y. Yi, Y. Guo, Z. Zuo, Y. Li, Z. Jia, H. Liu, Y. Li, Anchoring zero valence single atoms of nickel and iron on graphdiyne for hydrogen evolution, Nat. Commun. 9 (1) (2018) 1460–1470, https://doi.org/10.1038/s41467-018-03896-4.

[28] M. Wang, S. Liu, T. Qian, J. Liu, J. Zhou, H. Ji, J. Xiong, J. Zhong, C. Yan, Over 56.55% faradaic efficiency of ambient ammonia synthesis enabled by positively shifting the reaction potential, Nat. Commun. 10 (1) (2019) 1–8, https://doi.org/10.1038/s41467-018-08120-x.

[29] P. Huang, W. Liu, Z. He, C. Xiao, T. Yao, Y. Zou, C. Wang, Z. Qi, W. Tong, B. Pan, et al., Single atom accelerates ammonia photosynthesis, Sci. China Chem. 61 (9) (2018) 1187–1196, https://doi.org/10.1007/s11426-018-9273-1.

[30] F. Lü, S. Zhao, R. Guo, J. He, X. Peng, H. Bao, J. Fu, L. Han, G. Qi, J. Luo, et al., Nitrogen-coordinated single Fe sites for efficient electrocatalytic N_2 fixation in neutral media, Nano Energy 61 (5) (2019) 420–427, https://doi.org/10.1016/j.nanoen.2019.04.092.

[31] J. Jiao, R. Lin, S. Liu, W.C. Cheong, C. Zhang, Z. Chen, Y. Pan, J. Tang, K. Wu, S. F. Hung, et al., Copper atom-pair catalyst anchored on alloy nanowires for selective and efficient electrochemical reduction of CO_2, Nat. Chem. 11 (3) (2019) 222–228, https://doi.org/10.1038/s41557-018-0201-x.

[32] H. Yang, Y. Wu, G. Li, Q. Lin, Q. Hu, Q. Zhang, J. Liu, C. He, Scalable production of efficient single-atom copper decorated carbon membranes for CO_2 electroreduction to methanol, J. Am. Chem. Soc. 141 (32) (2019) 12717–12723, https://doi.org/10.1021/jacs.9b04907.

[33] J. Li, P. Pršlja, T. Shinagawa, A.J. Martín Fernández, F. Krumeich, K. Artyushkova, P. Atanassov, A. Zitolo, Y. Zhou, R. García-Muelas, et al., Volcano trend in electrocatalytic CO_2 reduction activity over atomically dispersed metal sites on nitrogen-doped carbon, ACS Catal. 9 (11) (2019) 10426–10439, https://doi.org/10.1021/acscatal.9b02594.

[34] W. Ju, A. Bagger, G.P. Hao, A.S. Varela, I. Sinev, V. Bon, B. Roldan Cuenya, S. Kaskel, J. Rossmeisl, P. Strasser, Understanding activity and selectivity of metal-nitrogen-doped carbon catalysts for electrochemical reduction of CO_2, Nat. Commun. 8 (1) (2017) 1–9, https://doi.org/10.1038/s41467-017-01035-z.

[35] Z. Zhang, C. Ma, Y. Tu, R. Si, J. Wei, S. Zhang, Z. Wang, J.F. Li, Y. Wang, D. Deng, Multiscale carbon foam confining single iron atoms for efficient electrocatalytic CO_2 reduction to CO, Nano Res. 12 (9) (2019) 2313–2317, https://doi.org/10.1007/s12274-019-2316-9.

[36] S. An, G. Zhang, T. Wang, W. Zhang, K. Li, C. Song, J.T. Miller, S. Miao, J. Wang, X. Guo, High-density ultra-small clusters and single-atom Fe sites embedded in graphitic carbon nitride (g-C_3N_4) for highly efficient catalytic advanced oxidation processes, ACS Nano 12 (9) (2018) 9441–9450, https://doi.org/10.1021/acsnano.8b04693.

[37] S.L. Li, H. Yin, X. Kan, L.Y. Gan, U. Schwingenschlögl, Y. Zhao, Potential of transition metal atoms embedded in buckled monolayer g-C_3N_4 as single-atom catalysts, Phys. Chem. Chem. Phys. 19 (44) (2017) 30069–30077, https://doi.org/10.1039/c7cp05195f.

[38] X. Chen, R. Hu, DFT-based study of single transition metal atom doped g-C_3N_4 as alternative oxygen reduction reaction catalysts, Int. J. Hydrogen Energy 44 (29) (2019) 15409–15416, https://doi.org/10.1016/j.ijhydene.2019.04.057.

[39] C. Yang, Z.Y. Zhao, H.T. Wei, X.Y. Deng, Q.J. Liu, DFT calculations for single-atom confinement effects of noble metals on monolayer g-C_3N_4 for photocatalytic applications, RSC Adv. 11 (7) (2021) 4276–4285, https://doi.org/10.1039/d0ra09815a.

[40] S. Pérez-Rodríguez, E. Pastor, M.J. Lázaro, Electrochemical behavior of the carbon black Vulcan XC-72R: influence of the surface chemistry, Int. J. Hydrogen Energy 43 (16) (2018) 7911–7922, https://doi.org/10.1016/j.ijhydene.2018.03.040.

[41] M. Navlani-García, D. Salinas-Torres, F.D. Vázquez-Álvarez, D. Cazorla-Amorós, Formic acid dehydrogenation attained by Pd nanoparticles-based catalysts supported on MWCNT-C_3N_4 composites, Catal. Today (2021), https://doi.org/10.1016/j.cattod.2021.07.019.

[42] W.J. Niu, J.Z. He, Y.P. Wang, Q.Q. Sun, W.W. Liu, L.Y. Zhang, M.C. Liu, M.J. Liu, Y. L. Chueh, A hybrid transition metal nanocrystal-embedded graphitic carbon nitride nanosheet system as a superior oxygen electrocatalyst for rechargeable Zn-air batteries, Nanoscale 12 (38) (2020) 19644–19654, https://doi.org/10.1039/d0nr03987j.

[43] X. Liu, W. Yang, L. Chen, Z. Liu, L. Long, S. Wang, C. Liu, S. Dong, J. Jia, Graphitic carbon nitride ($g\text{-}C_3N_4$)-derived bamboo-like carbon nanotubes/Co nanoparticles hybrids for highly efficient electrocatalytic oxygen reduction, ACS Appl. Mater. Interfaces 12 (4) (2020) 4463–4472, https://doi.org/10.1021/acsami.9b18454.
[44] A. Mishra, A. Mehta, S. Basu, N.P. Shetti, K.R. Reddy, T.M. Aminabhavi, Graphitic carbon nitride ($g\text{–}C_3N_4$)–based metal-free photocatalysts for water splitting: a review, Carbon 149 (2019) 693–721, https://doi.org/10.1016/j.carbon.2019.04.104.
[45] S. Patnaik, S. Martha, S. Acharya, K.M. Parida, An overview of the modification of $g\text{-}C_3N_4$ with high carbon containing materials for photocatalytic applications, Inorg. Chem. Front. 3 (3) (2016) 336–347, https://doi.org/10.1039/c5qi00255a.
[46] D. Lozano-Castelló, M.A. Lillo-Ródenas, D. Cazorla-Amorós, A. Linares-Solano, Preparation of activated carbons from Spanish anthracite - I. Activation by KOH, Carbon 39 (5) (2001) 741–749, https://doi.org/10.1016/S0008-6223(00)00185-8.
[47] S. Brunauer, P.H. Emmett, E. Teller, Adsorption of gases in multimolecular layers, J. Am. Chem. Soc. 60 (2) (1938) 309–319, https://doi.org/10.1021/ja01269a023.
[48] J. Jagiełło, Stable numerical solution of the adsorption integral equation using splines, Langmuir 10 (8) (1994) 2778–2785, https://doi.org/10.1021/la00020a045.
[49] J. Jagiello, J.P. Olivier, 2D-NLDFT adsorption models for carbon slit-shaped pores with surface energetical heterogeneity and geometrical corrugation, Carbon 55 (2) (2013) 70–80, https://doi.org/10.1016/j.carbon.2012.12.011.
[50] NLDFT Analysis by SAIEUS program, Retrieved from, http://www.nldft.com.
[51] American Elements, 10884 Weyburn Ave. Los Angeles, USA, Retrieved from, www.americanelements.com.
[52] R. Zhou, Y. Zheng, M. Jaroniec, S.Z. Qiao, Determination of the electron transfer number for the oxygen reduction reaction: from theory to experiment, ACS Catal. 6 (7) (2016) 4720–4728, https://doi.org/10.1021/acscatal.6b01581.
[53] Heine A. Hansen, Jan Rossmeisl, Jens K. Nørskov, Surface Pourbaix diagrams and oxygen reduction activity of Pt, Ag and Ni(111) surfaces studied by DFT, Phys. Chem. Chem. Phys. 10 (25) (2008) 3722–3730, https://doi.org/10.1039/b808799g.
[54] J.K. Nørskov, J. Rossmeisl, A. Logadottir, L. Lindqvist, J.R. Kitchin, T. Bligaard, H. Jónsson, Origin of the overpotential for oxygen reduction at a fuel-cell cathode, J. Phys. Chem. 108 (46) (2004) 17886–17892, https://doi.org/10.1021/jp047349j.
[55] T.S. Miller, A.B. Jorge, T.M. Suter, A. Sella, F. Corà, P.F. McMillan, Carbon nitrides: synthesis and characterization of a new class of functional materials, Phys. Chem. Chem. Phys. 19 (24) (2017) 15613–15638, https://doi.org/10.1039/c7cp02711g.
[56] J.M. Albella, A.M. Cintas, T. Miranda, J.M. Serratosa, Introducción a La Ciencia de Los Materiales: Técnicas de preparación y caracterización, CSIC, Madrid, Spain, 1993.
[57] E. Raymundo-Piñero, D. Cazorla-Amorós, A. Linares-Solano, J. Find, U. Wild, R. Schlögl, Structural characterization of N-containing activated carbon fibers prepared from a low softening point petroleum pitch and a melamine resin, Carbon 40 (4) (2002) 597–608, https://doi.org/10.1016/S0008-6223(01)00155-5.
[58] J.X. Flores-Lasluisa, J. Quílez-Bermejo, A.C. Ramírez-Pérez, F. Huerta, D. Cazorla-Amorós, E. Morallón, Copper-doped cobalt spinel electrocatalysts supported on activated carbon for hydrogen evolution reaction, Materials 12 (8) (2019) 1302–1315, https://doi.org/10.3390/ma12081302.
[59] F. Yang, X. Mao, M. Ma, C. Jiang, P. Zhang, J. Wang, Q. Deng, Z. Zeng, S. Deng, Scalable strategy to fabricate single Cu atoms coordinated carbons for efficient electroreduction of CO_2 to CO, Carbon 168 (2020) 528–535, https://doi.org/10.1016/j.carbon.2020.06.088.
[60] B. Wu, R. Yang, L. Shi, T. Lin, X. Yu, M. Huang, K. Gong, F. Sun, Z. Jiang, S. Li, L. Zhong, Y. Sun, Cu single-atoms embedded in porous carbon nitride for selective oxidation of methane to oxygenates, Chem. Commun. 56 (93) (2020) 14677–14680, https://doi.org/10.1039/d0cc06492k.
[61] A.P. Grosvenor, B.A. Kobe, M.C. Biesinger, N.S. McIntyre, Investigation of multiplet splitting of Fe 2p XPS spectra and bonding in iron compounds, Surf. Interface Anal. 36 (12) (2004) 1564–1574, https://doi.org/10.1002/sia.1984.
[62] Atkins, Overton, Rourke, Weller, Armstrong and Hagerman. Inorganic Chemistry, fifth ed., W. H. Freeman and Company, New York, 2010.
[63] J. Zhu, P. Xiao, H. Li, S.A.C. Carabineiro, Graphitic carbon nitride: synthesis, properties, and applications in catalysis, ACS Appl. Mater. Interfaces 6 (19) (2014) 16449–16465, https://doi.org/10.1021/am502925j.
[64] J.C. Cuevas, E. Scheer, The conductance of a single atom, in: J.C. Cuevas, E. Scheer (Eds.), Molecular Electronics in an Introduction to Theory and Experiment, World Scientific, London, 2017.
[65] J. Yang, W. Liu, M. Xu, X. Liu, H. Qi, L. Zhang, X. Yang, S. Niu, D. Zhou, Y. Liu, Y. Su, J.F. Li, Z.Q. Tian, W. Zhou, A. Wang, T. Zhang, Dynamic behavior of single-atom catalysts in electrocatalysis: identification of $Cu\text{-}N_3$ as an active site for the oxygen reduction reaction, J. Am. Chem. Soc. 143 (36) (2021) 14530–14539, https://doi.org/10.1021/jacs.1c03788.
[66] M.E. Vázquez, J.R. López, D. Medina-Rodelo, M. Jiménez-Edeza, G.M. Castañeda-Ruelas, A.M. López, J.M. Herrera-Ramírez, P.F. Méndez, Electrochemical study, structural characterization and antimicrobial activity of silver and copper oxide (CuO) nanoparticles synthesized by a green method using L-ascorbic acid and chitosan, Int. J. Electrochem. Sci. 14 (7) (2019) 6366–6375, https://doi.org/10.20964/2019.07.04.
[67] J. Zhang, X. Song, P. Li, S. Wang, Z. Wu, X. Liu, An iron-based catalyst with multiple active components synergetically improved electrochemical performance for oxygen reduction reaction, Catalysts 8 (6) (2018) 243–256, https://doi.org/10.3390/catal8060243.
[68] A. Gabe, R. Ruiz-Rosas, C. González-Gaitán, E. Morallón, D. Cazorla-Amorós, Modeling of oxygen reduction reaction in porous carbon materials in alkaline medium. Effect of microporosity, J. Power Sources 412 (2019) 451–464, https://doi.org/10.1016/j.jpowsour.2018.11.075.
[69] T.J. Bandosz, Revealing the impact of small pores on oxygen reduction on carbon electrocatalysts: a journey through recent findings, Carbon 188 (2022) 289–304, https://doi.org/10.1016/j.carbon.2021.11.071.
[70] U.I. Kramm, J. Herranz, N. Larouche, T. Arruda, M. Lefèvre, F. Jaouen, P. Bogdanoff, S. Fiechter, I. Abs-Wurmbach, S. Mukerjee, et al., Structure of the catalytic sites in Fe/N/C-catalysts for O_2-reduction in PEM fuel cells, Phys. Chem. Chem. Phys. 14 (33) (2012) 10715–10722, https://doi.org/10.1039/b000000x.
[71] T. Asset, P. Atanassov, Iron-nitrogen-carbon catalysts for proton exchange membrane fuel cells, Joule 4 (1) (2020) 33–44, https://doi.org/10.1016/j.joule.2019.12.002.
[72] R.A. Jasinski, New fuel cell cathode catalyst, Nature 201 (1964) 1212–1213.
[73] M. Lefèvre, E. Proietti, F. Jaquen, J.P. Dodelet, Iron-based catalysts with improved oxygen reduction activity in polymer electrolyte fuel cells, Science 324 (2009) 71–74, https://doi.org/10.1126/science.1170051.